Analysis of An Optical Wireless Receiver Using a Hemispherical Lens With Application in MIMO Visible Light Communications

Thomas Q. Wang, Y. Ahmet Sekercioglu, *Senior Member, IEEE*, and Jean Armstrong, *Senior Member, IEEE*

***Abstract*—White lighting LEDs offer great potential for high speed communications, especially for indoor applications. However, for their widespread adoption, two important issues need to be addressed: the lack of diversity in multiple-input multiple output (MIMO) systems, and the small field of view of receivers. In this paper, we describe a design using a hemispherical lens in the receiver that solves these problems. By using classical optics, we derive exact expressions for the channel gain and the optical power density of the projected images. Simulation results of a typical indoor scenario show that the new system has a wide field of view, and provides adequate channel gain for angles of incidence as large as 70 degrees. We present the distribution of optical power on the imaging plane for various receiving positions and tilted receivers over a number of representative indoor scenarios. They show that the images of LEDs are clearly distinguishable. The results demonstrate the presence of low channel correlations between individual transmitters and receivers. Consequently, this confirms that the new technique is capable of providing significant diversity order for MIMO optical wireless applications.**

***Index Terms*—Diversity, field of view, hemispherical lens, imaging receiver, intensity modulation and direct detection, MIMO, optical wireless communications, visible light communications.**

I. Introduction

VISIBLE LIGHT COMMUNICATION (VLC) is a promising solution for high speed data transmission in indoor applications. VLC was first proposed in Japan [1] and has since aroused significant interest around the world [2]–[4]. VLC possesses many advantages over its RF counterpart [4]. As the light cannot pass through opaque obstacles, the visible light band can be reused without any interference in different (even neighboring) rooms. The advantages of VLC also include: no licensing requirements, low-cost frontends, simultaneous illumination and communication, and high received signal-to-noise ratio (SNR). Additionally, as long as the eye-and-skin safety regulations are satisfied, there are no health concerns.

Many VLC systems use white LEDs as transmitters. Even though designed primarily for lighting, unlike conventional light sources, these white LEDs can be modulated at frequencies up to 20 MHz [5], and as a result, can form the basis of a range of novel data communication systems [6]–[13].

The most viable optical modulation and demodulation technology for optical wireless is intensity modulation and direct detection (IM/DD). In IM/DD systems, information is carried on the intensity of the light. Thus, all the transmitted information-carrying signals are nonnegative. In these optical systems the channel gain is given by the ratio of the received *optical power* to the transmitted *optical power* [14]. Therefore, unlike the complex gain of a RF channel, the channel gain of an optical wireless system is always real and positive. In the MIMO optical wireless context, multiple LEDs[1] act as transmitters emitting modulated signals, while multiple photodetectors detect the intensity of the received signals. Subsequently, as in MIMO RF channels, the optical wireless channels between the LEDs and the photodetectors can also be represented by a channel matrix [15]. However, unlike RF, the channel matrix for optical wireless is a real matrix with its elements denoting the power gains of all the LED-photodetector pairs.

Light propagating from each LED to the photodetector is generally made up of two components, the LOS component which transmits from the LED to the receiver directly and the diffuse component which propagates via reflections. Previous studies have shown that the LOS component is usually much stronger than the diffuse component [7], [16]. In this paper, we consider only the LOS component and leave the analysis of multi-path transmission for a future study.

In the context of optical wireless, receivers can be classified as 'imaging' or 'non-imaging' [7]. Recent research efforts have shown that the advantage of MIMO in non-imaging optical systems is relatively limited and that imaging receivers potentially offer better performance [7]. In the literature, two forms of MIMO imaging systems have been described [8], [9], [11]–[14]. In [8], a number of directional receivers are used. Although this arrangement provides diversity and therefore increases data rates, it is bulky and not easily scalable. The second form is based on standard camera technology [9], [12], [13]. Standard cameras are designed to have a field of view (FOV)

Manuscript received December 20, 2012; revised March 27, 2013; accepted March 31, 2013. Date of publication April 12, 2013; date of current version April 26, 2013. This work was presented in part at the 3rd IEEE Workshop on Optical Wireless Communications (OWC'12). This work was supported under an Australian Research Council's (ARC) Discovery funding scheme (DP 1094218).

The authors are with the Department of Electrical and Computer Systems Engineering, Monash University, Melbourne, VIC 3168, Australia (e-mail: Tom.Wang@monash.edu; Ahmet.Sekercioglu@monash.edu; Jean.Armstrong@monash.edu).

Color versions of one or more of the figures in this paper are available online at http://ieeexplore.ieee.org.

Digital Object Identifier 10.1109/JLT.2013.2257685

[1]Although LED light fittings are often made up of multiple LEDs, to simplify the discussion in this paper we assume each light fitting has only one LED which acts as a point source.

that matches the human eye, and to produce focused images [17]. This is in contrast to MIMO optical wireless, where, in many cases, a much wider FOV is desirable. In order to provide adequate illumination throughout an area, rooms are usually equipped with a number of lights spaced at intervals on the ceiling. A receiver that has a wide FOV and therefore, has LOS to most or all of these lights will be able to support higher data rate communications than one with a narrow FOV that has LOS to only some of them.

A hemispherical lens can provide a very wide FOV. Its application to sky cloud coverage recording studies can be traced back as early as 1920 s [18]. Even though lenses with wide FOV produce distorted images, which can be considered as a limitation in photography and image processing, this is not a problem for MIMO IM/DD optical wireless applications. In [19], we show the wide FOV and the significant diversity order achieved by an imaging receiver using a hemispherical lens. In this paper, we present a more in-depth and comprehensive study of this receiver setup and the corresponding MIMO channels by extending the previous work [19] to two more general scenarios: an asymmetric arrangement and a tilted receiver. The power density of ambient light is also included in this study by modeling the sources as many LEDs located on a hemispherical dome co-centered with the hemispherical lens of the receiver. We first derive an expression for the channel gain of an optical system with a single photodetector, providing the relationship between the transmitted and received power. Then, we extend the study to multiple photodetectors. We calculate the power density which shows the optical power distribution on the receiver plane geometrically. Based on these, the channel gain for a given LED/photodetector pair can be calculated by integrating the power density generated by the LED over the area of the photodetector. The simulation results show that the imaging receiver can

1) receive the light signal from a large range of angles of incidence, and
2) effectively separate the signals from different LEDs.

The very large FOV enables LOS communications in more cases than otherwise would be possible, and thus improves the SNR at the photodetector. Effective separation of signals reduces the correlations between the elements of the channel matrix. The low correlations between the elements of the channel matrix provide spatial diversity for the efficient decoding of the signal in a MIMO system.

II. System Description

Consider the imaging system shown in Fig. 1. Here, N_t white LED ceiling lights illuminate a room and transmit data. The receiver mechanism is composed of two parts—a hemispherical lens to refract the emitted light, and an array of N_r photodetectors.

The photodetectors can be in the form of the individual pixels of a camera sensor, in which case the photodetector array may have a very large number of elements, or alternatively a small number of individual photodetectors can be used.

Let $\mathbf{H}$ be the $N_r \times N_t$ channel matrix between the LEDs and the photodetectors. The element $\mathbf{H}(i,j)$ represents the channel gain between the ith photodetector and the jth LED.

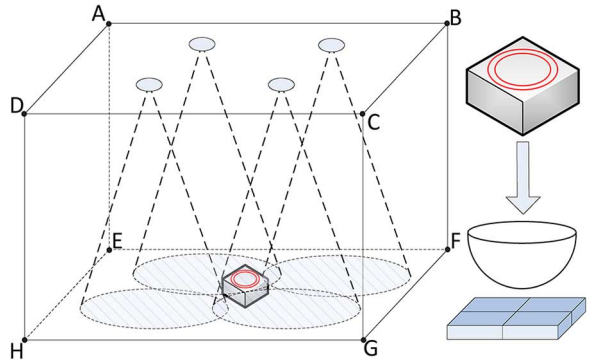

Fig. 1. Schematic diagram of the imaging system configuration for MIMO optical wireless communication. The LEDs are installed on the ceiling and pointing down, the receiver setup is placed on the floor.

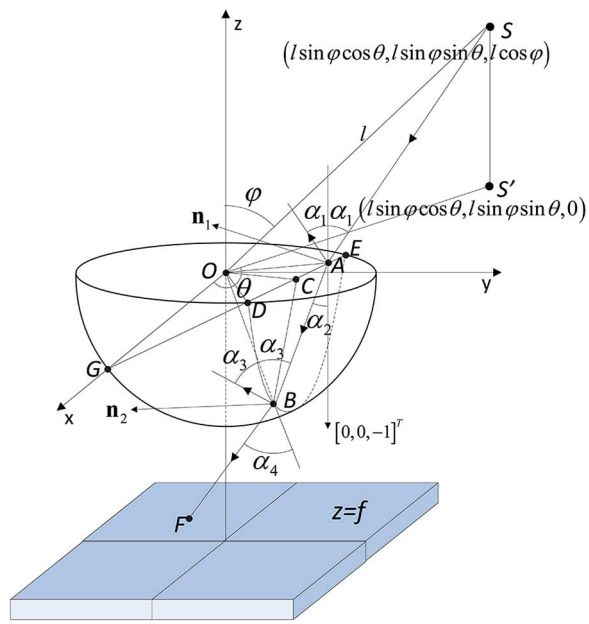

Fig. 2. Geometrical model of the receiver setup consisting of a hemispherical lens and a photodetector array.

Fig. 2 shows the geometrical model of the receiver using a spherical coordinate system. A LED is placed at point $S : (l\sin\varphi\cos\theta, l\sin\varphi\sin\theta, l\cos\varphi)$, directed downwards and emits unpolarized white light. The origin of the coordinate system is at the center of the flat surface of the hemispherical lens which is on the xOy plane. Note that the xOy plane is not necessarily parallel to the floor as the receiver may be tilted. Thus, by definition of the spherical coordinate system,l, φ and θ represent the distance to the center of the flat surface of the lens, the angle between SO and the positive z axis, and the angle between $S'O$ and the positive x axis, respectively. We assume that the LED is at a distance much greater than R, the radius of the lens (i.e., $l \gg R$). Thus, we can assume that all the light rays coming from the LED arrive at the flat surface of the lens with almost the same angle of incidence, $\alpha_1 = \varphi$, after travelling the same distance, l (i.e., SO can be regarded as (approximately) parallel to SA in Fig. 2). After passing through the lens, the refracted rays hit the photodetector array which is located on the imaging (receiver) plane $z = f$, $f < -R$ and

form the image of the LED. The optical power received by the photodetector array generates the photocurrent which is used for detection.

III. System Analysis

In this section, we present an analysis of the system. First we calculate the channel gain for a single photodetector and then extend this to the case of multiple photodetectors. For the single photodetector, the channel gain for a given LED is found by calculating the total power of the light which passes through the lens and reaches the imaging plane when that LED is transmitting unity optical power. To extend the results to the case of multiple photodetectors, the distribution of the received power on the receiver plane must be calculated first. Then the power received by each photodetector is evaluated by integrating the power density over the area of the photodetector. In order to find the distribution of the received power, we treat the light emitted from a given LED as rays each of which hits an infinitesimal area on the flat surface of the lens. Then we apply classical optics and 3-D geometry to each ray to find (i) how much power each ray has when it reaches the imaging plane and (ii) where each ray strikes the imaging plane after the refraction of the lens. In the analysis, we consider a ray hitting an arbitrary point A on the flat surface of the lens, passing through the lens at point B and finally getting to point F on the imaging plane as shown in Fig. 2. We calculate the optical power at F using the Fresnel equations and find the coordinates of F using 3-D geometry.

First, consider the situation where there is a single LED transmitting data and a single photodetector which is large enough to collect all of the light refracted through the lens. The LED and the photodetector form a single-input single-output (SISO) system. Thus, the channel gain is the ratio of the total received optical power on the photodetector to the transmitted optical power, which is given by the following theorem.

Theorem 1: The channel gain of the system is given by

$$\begin{aligned} T &= \frac{P_o}{P_t} \\ &= \frac{(m+1)\cos^m\phi\cos\varphi}{2\pi l^2} \times T_{\mathrm{air-lens}}(\alpha_1,\alpha_2) \\ &\quad \times \int\int_{\alpha_3<\arcsin\left(\frac{n_1}{n_2}\right)} T_{\mathrm{lens-air}}(\alpha_3,\alpha_4) r dr d\beta. \end{aligned} \tag{1}$$

Here, P_o is the optical power received at the photodetector, and P_t is the power emitted by the LED. $T_{\mathrm{air-lens}}(\alpha_1,\alpha_2)$ and $T_{\mathrm{lens-air}}(\alpha_3,\alpha_4)$ are the power transmission coefficients of the air-lens surface (flat surface) and the lens-air surface (spherical surface), respectively. ϕ is the angle of emission relative to the optical axis of the emitter and $m = -\ln 2/\ln(\cos\Phi_{1/2})$ where $\Phi_{1/2}$ is the half power semi-angle of the LED. α_2 is the angle of refraction of the flat surface and α_3 and α_4 are the angles of incidence and refraction of the curved (spherical) surface. r and β are the radius and polar angle for the polar coordinates on the xOy plane.

In (1), the first term represents the irradiance on the flat surface of the lens, the second term represents the proportion of light which passes through the flat surface of the lens, while the final term represents transmission through the curved surface. Because the transmission at the curved surface depends on the angle at which the light reaches the curved surface, which in turn depends on the point the ray hits the flat surface, the final term is in the form of an integral. The proof of Theorem 1 is given in Appendix I.

Now, we extend the discussion to multiple photodetectors. In order to calculate the power that an individual photodetector receives from the LED, we need to trace all the light rays which are emitted by the LED and reach the photodetector under consideration. To do this, we need to calculate not only the received power due to each ray but also the coordinates of F at which that ray intersects with the receiver plane on which the photodetector array is placed. From this, the total power received by each photodetector can be calculated by integrating the optical power density over the area of that photodetector. Finally, noting that the total power on each photodetector is just the superposition of the power from each LED, the extension to MIMO is quite straightforward.

Consider a ray which passes through the lens after hitting the flat and curved surfaces of the lens at points A and B respectively, and intersects with the imaging plane at point F as shown in Fig. 2. Then, given the coordinates of $A:(r\cos\beta, r\sin\beta, 0)$, the power density at point F can be derived readily from (23) to give

$$\begin{aligned} &\frac{dP_o}{dA} \\ &= \frac{P_t(m+1)\cos^m\phi\cos\varphi}{2\pi l^2} T_{\mathrm{air-lens}}(\alpha_1,\alpha_2) T_{\mathrm{lens-air}}(\alpha_3,\alpha_4), \end{aligned} \tag{2}$$

where $dA = rdrd\beta$.

The calculation of the coordinates of F is done in three steps using three dimensional geometry. First the coordinates of point B (see Appendix III) and the angle α_4 (see Appendix II) are calculated, next these are used to derive the equation for line BF, finally, using the fact that F lies on the plane $z = f$, the coordinates of F are calculated.

Denote the unit vector with direction pointing from M_1 to M_2 by $\mathbf{r}_{M_1M_2}$, i.e.

$$\mathbf{r}_{M_1M_2} = \frac{[x_{M_2}-x_{M_1}, y_{M_2}-y_{M_1}, z_{M_2}-z_{M_1}]^T}{|M_1M_2|}, \tag{3}$$

where x_{M_i}, y_{M_i} and z_{M_i}, $i = 1, 2$ denote the Cartesian coordinates of point M_i and "$|\cdot|$" denotes the magnitude of the vector. Moreover, we define two unit vectors $\mathbf{n}_1$ and $\mathbf{n}_2$ given by

$$\mathbf{n}_1 = \frac{[0,0,-1]^T \times \mathbf{r}_{SA}}{\sin\alpha_1} = [-\sin\theta, \cos\theta, 0]^T \tag{4}$$

and

$$\mathbf{n}_2 = \frac{\mathbf{r}_{OB} \times \mathbf{r}_{AB}}{\sin\alpha_3}, \tag{5}$$

respectively, where "$\times$" denotes the cross product of the vectors. Since point F is the intersection of the straight line BF and the plane $z = f$, (see Fig. 2), its coordinates can be derived by substituting $z = f$ into the function of the straight line BF which is determined by the coordinate of point B and the vector

of direction cosines $\mathbf{r}_{BF}$. The following theorem presents the calculation of these parameters using Euler-Rodrigues formula [23].

Theorem 2: Given the ray coming from $S : (l\sin\varphi\cos\theta, l\sin\varphi\sin\theta, l\cos\varphi)$ and reaching point $A : (r\cos\beta, r\sin\beta, 0)$, the refracted ray (from the flat surface) will hit the curved surface of the lens at B whose coordinates are given by:

$$\begin{aligned} x_B &= -t\sin\alpha_2\cos\theta + r\cos\beta \\ y_B &= -t\sin\alpha_2\sin\theta + r\sin\beta, \\ z_B &= -t\cos\alpha_2 \end{aligned} \tag{6}$$

where

$$t = r\sin\alpha_2\cos(\theta-\beta) + \sqrt{r^2\sin^2\alpha_2\cos^2(\theta-\beta) + R^2 - r^2}, \tag{7}$$

with the direction of refracted ray (of curved surface) given by $\mathbf{r}_{BF} = \mathbf{R}_2\mathbf{r}_{OB}$, where the matrix $\mathbf{R}_2$ can be expressed as

$$\mathbf{R}_2 = \cos\alpha_4\mathbf{I} + (1-\cos\alpha_4)\mathbf{A}_2 + \sin\alpha_4\mathbf{B}_2, \tag{8}$$

with $\mathbf{A}_2$ and $\mathbf{B}_2$ being 3×3 matrices and relative to the axis vector $\mathbf{n}_2$ by

$$\mathbf{A}_2 = \begin{bmatrix} \mathbf{n}_2^2(1) & \mathbf{n}_2(1)\mathbf{n}_2(2) & \mathbf{n}_2(1)\mathbf{n}_2(3) \\ \mathbf{n}_2(2)\mathbf{n}_2(1) & \mathbf{n}_2^2(2) & \mathbf{n}_2(2)\mathbf{n}_2(3) \\ \mathbf{n}_2(3)\mathbf{n}_2(1) & \mathbf{n}_2(3)\mathbf{n}_2(2) & \mathbf{n}_2^2(3) \end{bmatrix} \tag{9}$$

and

$$\mathbf{B}_2 = \begin{bmatrix} 0 & -\mathbf{n}_2(3) & \mathbf{n}_2(2) \\ \mathbf{n}_2(3) & 0 & -\mathbf{n}_2(1) \\ -\mathbf{n}_2(2) & \mathbf{n}_2(1) & 0 \end{bmatrix}. \tag{10}$$

The proof of Theorem 2 is given in Appendix III. Therefore, the function of straight line BF can be expressed as

$$\frac{x-x_B}{\mathbf{r}_{BF}(1)} = \frac{y-y_B}{\mathbf{r}_{BF}(2)} = \frac{z-z_B}{\mathbf{r}_{BF}(3)}. \tag{11}$$

Since the photodetector is located on the plane $z=f$, the coordinates can be calculated by substituting $z=f$ into (11), to give the coordinates of F

$$\begin{aligned} x_F &= \mathbf{r}_{BF}(1)\left(\frac{f-z_B}{\mathbf{r}_{BF}(3)}\right) + x_B \\ y_F &= \mathbf{r}_{BF}(2)\left(\frac{f-z_B}{\mathbf{r}_{BF}(3)}\right) + y_B. \\ z_F &= f \end{aligned} \tag{12}$$

IV. Simulation Results and Discussions

We now present simulation results for a $5\text{ m}\times 5\text{ m}\times 2.5\text{ m}$ room with four LED transmitters on the ceiling pointing down as shown in Fig. 1. The top view of the configuration is shown in Fig. 3 in which the four LEDs are installed at $T_x^{(1)} : (4,4,2.5)$, $T_x^{(2)} : (1,4,2.5)$, $T_x^{(3)} : (1,1,2.5)$ and $T_x^{(4)} : (4,1,2.5)$ in coordinate system $\hat{x}\hat{O}\hat{y}$ whose origin is located at point E. Five

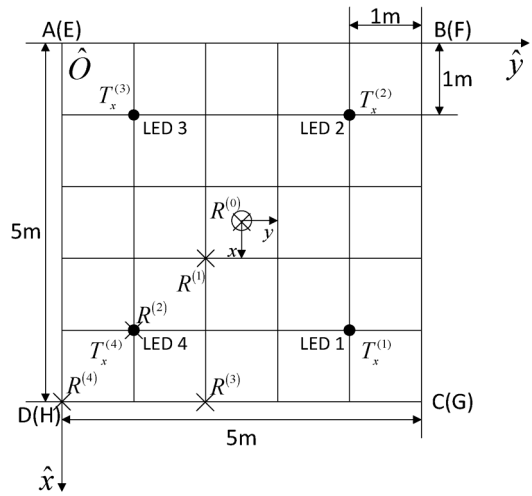

Fig. 3. Top view of the configuration used in the simulations.

receivers (marked by "x") are positioned at $R^{(i)} : (\hat{x}_i, \hat{y}_i, -z)$, $i = 0,\cdots,4$.

We initially consider the case where the receivers are pointing directly up. For each receiver we consider a coordinate system xOy originating at the center of the flat surface of the lens. x and y axis are parallel to $\hat{x}$ and $\hat{y}$ axis, respectively. (To extend the results to a tilted receiver we later apply a rotation relative to this initial position.) Therefore, given any point $(\hat{u},\hat{v},\hat{w})$ and the position of the receiver $(\hat{x}_i,\hat{y}_i,-z)$ in coordinate system $\hat{x}\hat{O}\hat{y}$, the coordinates of the point in coordinate system xOy are $(\hat{u}-\hat{x}_i, \hat{v}-\hat{y}_i, \hat{w}+\hat{z})$ from which the angle of incidence, α_1, the angle, θ, and the distance, l, can readily be derived. When the receiver is tilted, the corresponding coordinates can be calculated using Euler-Rodrigues formula [23].

We consider a hemispherical lens with a diameter of 5 mm and the index of refraction of 1.5. The lens is placed above the imaging plane at a distance of $-z$, $-z \ll 2.5$ m from the flat surface of the lens to the imaging plane. Consequently, the distance from the flat surface of the lens to the ceiling is approximately 2.5 m. Therefore, we can calculate that the angle of incidence, α_1, achieves its maximum at 70.5 degrees when a LED is placed at one of the corners of ceiling and the imaging plane at the furthest corner on the floor.

A. Channel Gain

First, we study the channel gain of a SISO system. The single photodetector is pointing up and assumed to be large enough to collect all the light passing through the lens. Note that, in this indoor environment, the distance, l, changes when we increase, or decrease, the angle of incidence, α_1. In Fig. 4, channel gains versus the angle of incidence are plotted for various generalized Lambertian LEDs. The half power semi-angles considered are $\Phi_{1/2} = 15°$, $30°$, $45°$ and $60°$, respectively. Without loss of generality, we normalize the transmitted power to unity. Thus, the received power on the photodetector indicates the channel gain. As shown in Fig. 4, all the channel gains decrease dramatically with the angle of incidence. This is because (i) the

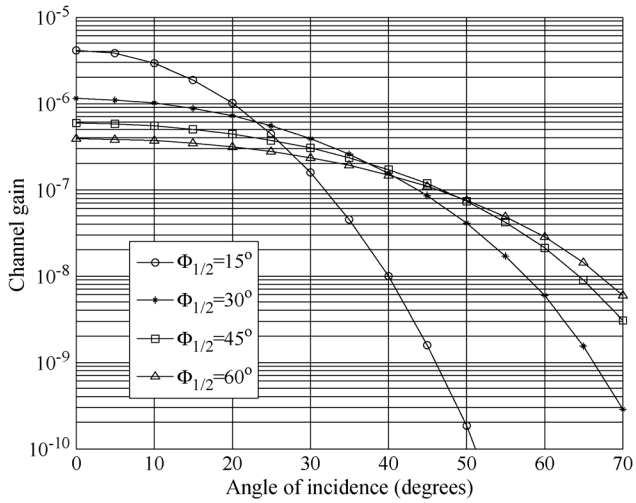

Fig. 4. Channel gains versus the angle of incidence for Lambertian emitters with varying half power semi-angles in the room shown in Fig. 1.

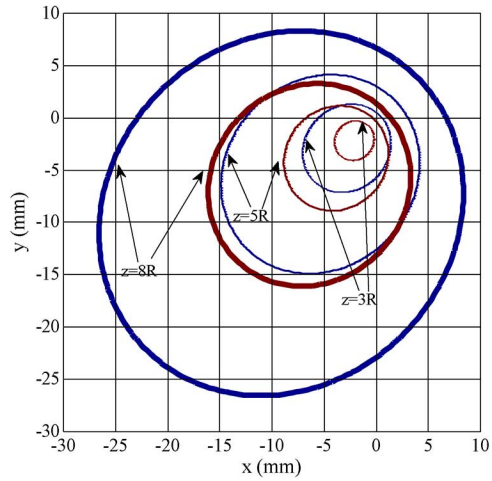

Fig. 5. Contour plots with various imaging plane positions.

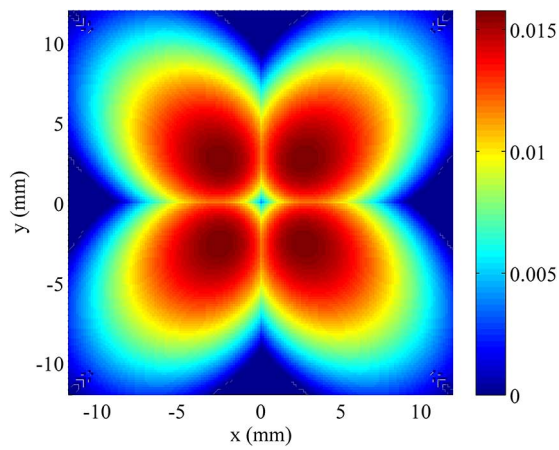

Fig. 6. Power density on the imaging plane.

reflection coefficient of the lens increases with the angle of incidence, and (ii) the effective area of the flat surface of the lens changes in proportion to $\cos\alpha_1$. Since the LED with higher directionality transmits more power in the direction of its axis, the LEDs with smaller $\Phi_{1/2}$ (15° and 30°) provide larger channel gain than the ones with lower directionality when the angle of incidence is small, say less than 23 degrees in this figure. However, as the angle of incidence increases, less power reaches the lens for the emitter with small $\Phi_{1/2}$ than for the ones with large $\Phi_{1/2}$ (lower directionality). As a result, the channel gain of the LEDs with high directionality falls much more rapidly than the other LEDs. Fig. 4 also shows that the LED with 60 degrees semi-angle provides the highest channel gain for angles of incidence greater than 45 degrees. In this case, the imaging system can provide a very wide effective FOV.

B. Power Density With Various Imaging Plane Positions

Now, we study the power density formed on different imaging planes for the case where the receivers point directly up. A LED is positioned at ($l = 2.5/\cos\varphi$, $\varphi = 30°$, $\theta = 45°$) and three imaging plane positions are considered at $z = -3$ R, $z = -5$ R and $z = -8$ R, respectively. In Fig. 5, three pairs of contour lines are plotted. The peak value of power density for a given imaging plane is used as the reference for that plane. The inner circle denotes the contour plots of 90% of the peak value and the outer ones 50%. For the contour plots with the same percentage of the peak value in the three planes, the image on the plane which has the longest distance from the lens ($z = -8$ R) covers a large area, while the contour plot for the nearest plane encloses a smaller area (see $z = -3$ R). Moreover, although the contour plots have different sizes, the outlines have similar shapes. In the rest of this paper, we consider the imaging plane located at $z = -3$ R.

C. Power Density With Symmetrical Arrangement

We study the power density at the imaging plane by first considering a symmetrical arrangement. We put the receiver pointing up at the center of the room $R(0)$. Thus, the angle of incidence, α_1, is the same for all LEDs and equals 40.4°. The four LEDs are of 60° of semi-angle. We plot the optical power density generated on the imaging plane in Fig. 6. As shown in the figure, the signals from different LEDs are clearly separated, with the images of $T_x^{(1)}$, $T_x^{(2)}$, $T_x^{(3)}$ and $T_x^{(4)}$ mainly located at the third, the fourth, the first and the second quadrant, respectively. Therefore the majority of the power emitted from a given LED is received by its corresponding quadrant. To demonstrate the diversity that can be achieved we consider the case where there are four photodetectors, and each photodetector collects all of the light in one of the quadrants of Fig. 6. The channel matrix for this configuration was calculated by integrating the received power density due to each LED over each quadrant to give

$$\mathbf{H} = \begin{bmatrix} 0 & 0.053 & 1.130 & 0.053 \\ 0.053 & 0 & 0.075 & 1.152 \\ 1.174 & 0.076 & 0.001 & 0.076 \\ 0.053 & 1.152 & 0.075 & 0 \end{bmatrix} \times 10^{-6} \qquad (13)$$

Note that in each row or column, there is one element which is much larger than the others. This indicates that (i) for a given photodetector, almost all the power it receives comes from a single LED and (ii) for a given LED, almost all of the power

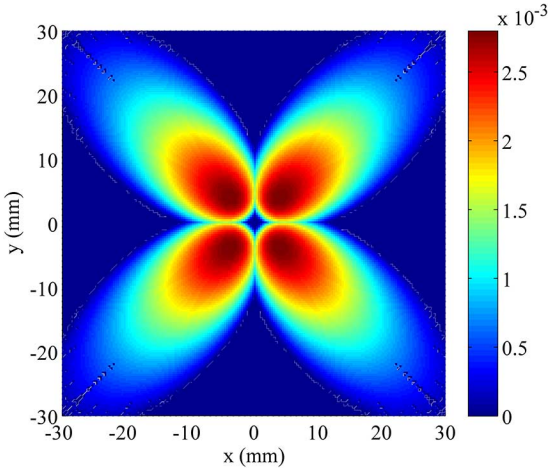

Fig. 7. Power density on the imaging plane with 60 degrees of the angle of incidence.

that passes through the lens is received by a single photodetector. Therefore, there is little correlation between the rows (columns) of the channel matrix when the new system is used. The resulting channel matrix is invertible even though there is interchannel interference. Thus, the transmitted data can be decoded by using the method described in [7]. Consequently, the new technique can form the basis of MIMO systems with high spatial diversity.

On the contrary, the spatial diversity is difficult to achieve for a non-imaging receiver [7]. Since the size of the photodetector array is usually much smaller than the distance l, in a non-imaging receiver the rays from any given LED can be regarded as parallel as they reach the photodetectors. The distance from each photodetector to a LED varies very little. From [14], we can see that the irradiance each photodetector receives from a given LED would be almost identical. This results in a channel matrix in which the columns are highly correlated. In the worst case, the rank of the matrix in a non-imaging receiver may decrease to 1, which leads to a very high bit error rate (BER) as in [7].

We also consider the effect of placing the LEDs further apart so that the angles of incidence for the light rays increase. Fig. 7 shows the result for $\varphi = 60°$. As can be seen from the figure, the images of the four LEDs are now completely distinct. In this situation, the columns of the channel matrix are orthogonal. Thus, the normalized form of the channel matrix can be expressed as

$$\mathbf{H} = \begin{bmatrix} 0 & 0 & 1 & 0 \\ 0 & 0 & 0 & 1 \\ 1 & 0 & 0 & 0 \\ 0 & 1 & 0 & 0 \end{bmatrix} \tag{14}$$

Eq. (14) and Fig. 7 show that each photodetector receives a signal from only a single LED. Thus, the received signal at each photodetector comprises only the signal from its corresponding LED plus the ambient light. As a result, there is no interchannel interference between the channels. Note that the orthogonal structure of the channel matrix also reduces the decoding complexity. Since each photodetector receives signal only from its corresponding LED, decoding can be performed as in a SISO system without interference.

Preliminary empirical results obtained using an experimental setup for a symmetrical arrangement [24] show very close agreement with the theoretical study presented here.

D. Power Density With Asymmetrical Arrangement

Next, we place the receiver at positions $R^{(1)}$, $R^{(2)}$, $R^{(3)}$ and $R^{(4)}$ in Fig. 3 and study the power density of these asymmetrical arrangements. From Fig. 3, we can observe that $R^{(1)}$ is located near the center of the room while $R^{(3)}$ and $R^{(4)}$ are near a wall and corner, respectively. $R^{(2)}$ is right below LED $T_x^{(4)}$. Fig. 8 contains the images observed for receivers at these points. Contour plots are included to indicate the outline of these images. Note that due to the asymmetrical arrangement, the images are no longer symmetrical with respect to the center and that the different subplots in Fig. 8 use different axes. Some images are brighter than the others because of the lower attenuations of their channels. However, as shown in the figures, the images are still very well separated, so a MIMO system with this configuration can have a high diversity order. However, to achieve significant diversity, more photodetectors may be required. In Fig. 8(a), the images formed for a receiver at $R^{(1)}$ are plotted. As the receiver is located near the center of the room, as with the symmetrical arrangement, the images are separated clearly with most of the power distributed within their corresponding quadrant. So, four detectors arranged as described in Section IV-C, where each photodetector collects all of the light in one quadrant, would provide good diversity. Fig. 8(b) plots the images formed for a receiver at $R^{(2)}$. The bright circular image is generated by LED $T_x^{(4)}$ since it is the nearest LED and it also has the smallest angle of incidence. Because the LED $T_x^{(2)}$ is the most distant and also has the largest angle of incidence among the LEDs, the channel from $T_x^{(2)}$ to the receiver suffers the greatest attenuation, and as a result there is very low channel gain and power density on the imaging plane. Nevertheless, part of its image is still well separated from other images. However, the images are not centered in different quadrants, so the simple arrangement of four detectors would not provide adequate diversity and more photodetectors are required. Fig. 8(c) and (d) are plotted at $R^{(3)}$ and $R^{(4)}$, respectively. As both of the points are located far away from the center of the room, optical channels of distant LEDs are seriously attenuated. In Fig. 8(c), the light from $T_x^{(1)}$ and $T_x^{(4)}$ is received with relatively large power density and the images are clearly separated. In Fig. 8(d), the channel condition for $T_x^{(4)}$ is favorable due to the short distance and small angle of incidence. Thus a relatively high power signal is received from $T_x^{(4)}$. However, because of the long propagation distances, the channel attenuation for the other LEDs increases and the images of those LEDs have reduced power.

E. Power Density of Tilted Receiver

We now consider the case where the receiver is tilted and is no longer horizontal. The receiver is placed at $R^{(3)}$ and $R^{(4)}$, respectively. At $R^{(3)}$, the flat surface of the lens is rotated clockwise by 45 degrees about the $\hat{y}$ axis. At $R^{(4)}$, we rotate the receiver clockwise first about $\hat{x}$ axis by 45 degrees and then

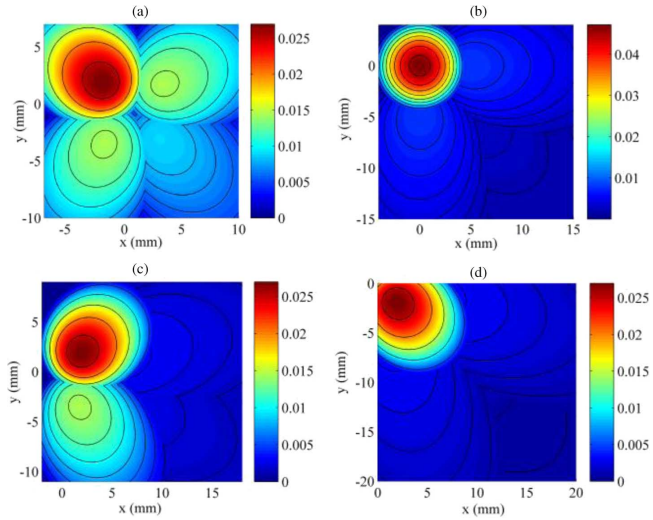

Fig. 8. Power density on the imaging planes at various locations with receiver pointing up. (a) Power density at $\mathrm{R}^{(1)}$; (b) Power density at $\mathrm{R}^{(2)}$; (c) Power density at $\mathrm{R}^{(3)}$; (d) Power density at $\mathrm{R}^{(4)}$.

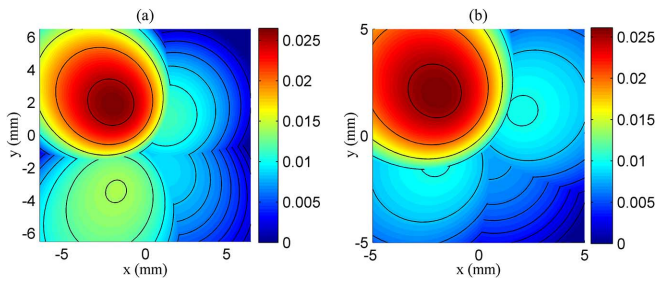

Fig. 9. Power density on the imaging planes at $R^{(3)}$ and $R^{(4)}$. (a) Power density at $\mathrm{R}^{(3)}$; (b) Power density at $\mathrm{R}^{(4)}$.

about $\hat{y}$ axis by 45 degrees. In Fig. 9(a) and (b), power density is plotted at $R^{(3)}$ and $R^{(4)}$, respectively. From the figure, it can be observed that the images are still well separated. Note that, as the receiver is tilted to point to the LEDs more directly, the distant LEDs have more favorable optical channels than in Fig. 8.

F. Power Density of Ambient Light

Shot noise induced by ambient light is the dominant component of the noise at the receiver since most optical wireless systems operate in the presence of high ambient light levels. We present the image of the ambient light formed by the hemispherical lens to study the power distribution of the shot noise on the imaging plane. Here, we consider the case where the ambient light comes from all directions and creates identical irradiance at every point on the flat surface of the lens. Therefore, this can be conceptually modeled as infinite number of light sources distributed uniformly on the inner surface of a hemispherical dome, co-centered with the flat surface of the lens and pointing towards the receiver. Since the size of the lens is much smaller than the dome, the irradiance is approximately identical at any point on the flat surface of the lens. For our simulation, we divide the lighting dome into 1 000 000 small sections, each of which works as a source of ambient light. The resulting relative power density is plotted in Fig. 10 in which Fig. 10(a)

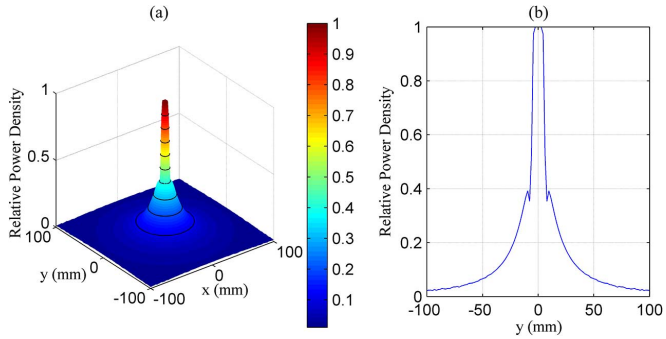

Fig. 10. Relative power density of ambient light. (a) 3-D Power density; (b) 2-D Power density.

describes the 3-D relative power density on the imaging plane and Fig. 10(b) shows the 2-D relative power density versus the distance to the center when x equals 0. From Fig. 10, we can observe that the power of shot noise is mainly distributed near the center of the imaging plane, and the power density drops dramatically as the distance from the center increases. This indicates that the lens focuses the ambient light coming from all directions onto a small area at the center of the imaging plane. For a lens with a diameter of 5 mm, the power of ambient light is observed to be distributed in a circular area with a diameter of 100 mm.

G. Spatial Diversity of Practical Systems

The analysis and simulations have shown that the new system can form the basis of a MIMO system with good spatial diversity. In this section, we discuss the limitations of the analysis and the implications for the design of practical systems using the new technique.

To make the analysis tractable, we made the following assumptions:

1) There is only LOS (not diffuse) transmission between each LED and the flat surface of the lens.
2) Each LED is a point source.
3) The rays from a given LED are approximately parallel when they reach the flat surface of the lens.
4) Power is lost only at the surfaces of the lens through reflection (not within the lens through dissipation).
5) Light reflected internally at the curved surface of the lens is lost from the system and does not reach the photodetector array after multiple reflections.
6) All of the light reaching the photodetecting array is detected.

Previous studies [7], [16] have shown that the LOS component is usually much stronger than the diffuse component so in most cases the first assumption will apply in practical configurations. Assumptions 2 and 3 depend on the relative size of the light fitting, the room, and the lens. Because the dimensions of the room are much larger than those of the lens, the assumptions will be accurate for light fittings with small dimensions. For very large light fittings which subtend a significant angle at the surface of the lens, the system would still have significant spatial diversity but the analysis and simulations would have to be modified to include the size of the light.

The amount of light dissipation within the lens (assumption 4) depends on the material used to make the lens, but while this will have some effect on the overall attenuation, it will only have second order effects on the diversity.

In the analysis and simulations, the effect of multiple internal reflections was ignored. The power of this component will be small, but it will reduce the diversity of the system slightly as light from a given LED will reach the photodetecting surface at the 'wrong' point. Finally it was assumed that all of the light reaching the photodetecting array is detected. Practical photodetectors have a limited FOV. This means that light that hits the photodetector array at an oblique angle will not be detected. For the configurations we have considered this effect is negligible.

The analysis and simulation have shown that even for quite extreme cases the images of different LEDs on the photodetecting plane are well separated. As a result, the limitation on diversity in practice will be the number of photodetecting elements and the sophistication of the signal processing used to combine inputs from different photodetectors. The image of a given LED depends on the angle of incidence α_1. Thus the most difficult images to separate are from LEDs with similar angles of incidence. A practical example of this would be two LEDs close together in one corner of the room and the receiver at the opposite corner. A greater number of photodetecting elements would be required to provide significant spatial diversity in this case.

V. Conclusion

In this paper, we present an analysis of an imaging MIMO optical wireless system which uses a hemispherical lens in the receiver setup. The channel gain and the power density of the new system are derived. We show that the system provides a wide FOV and significant spatial diversity at the same time. Results are presented for a number of typical indoor optical wireless scenarios. The plot of channel gain versus angle of incidence demonstrates the wide field of view of the system which provides adequate channel gain for angles of incidence even as large as 70 degrees. The power density is also plotted for scenarios of symmetrical and asymmetrical arrangements including the tilted receiver. For symmetrical arrangements, the channel matrix for a 4×4 MIMO system is calculated showing that the system has significant spatial diversity. For asymmetrical arrangements, although some of the optical channels are seriously attenuated due to long propagation distance and large angles of incidence, the images are still shown to be separated effectively. The separation of the images leads to low correlation between the elements of channel matrix and therefore a full-ranked channel matrix. Consequently, significant diversity order and wide FOV can be provided by the imaging receiver which can be used for high data rate communications.

Appendix I

Proof of Theorem I: The channel gain for the single photodetector case, depends only on how much light is reflected and reflected at each surface, which in turn depends only on the angles α_1 and α_3 at which a given ray reaches the flat and curved surfaces. In this appendix, the channel gain is calculated in terms of α_1 and α_3.

Given the parameters $P_t, \phi, m, l, \varphi, \theta$ regarding the transmission pattern, the location of the LED and the polar coordinates $A : (r\cos\beta, r\sin\beta, 0)$ where the ray arrives at the flat surface of the lens, the power dP_1 received at an infinitesimal area $rdrd\beta$ centered at A can be expressed as [14]

$$\begin{aligned} dP_1 &= \frac{P_t R_o(\phi) r dr d\beta \cos\varphi}{l^2} \\ &= \frac{P_t(m+1)\cos^m\phi\cos\varphi}{2\pi l^2} r dr d\beta, \end{aligned} \tag{15}$$

where

$$R_o(\phi) = \frac{(m+1)}{2\pi}\cos^m\phi, \tag{16}$$

denotes the generalized Lambertian radiation pattern [14], [20]. Due to reflections, power of the light rays is partially lost. The proportion of the light, which is reflected, depends on the angle of incidence, $\alpha_1 = \varphi$, the refractive indices n_1 (for the air) and n_2 (for the lens), and is given by the Fresnel equations [21]

$$R_{\mathrm{p}}(\alpha_1, \alpha_2) = \frac{n_1\cos\alpha_2 - n_2\cos\alpha_1}{n_1\cos\alpha_2 + n_2\cos\alpha_1} \tag{17}$$

and

$$R_{\mathrm{s}}(\alpha_1, \alpha_2) = \frac{n_1\cos\alpha_1 - n_2\cos\alpha_2}{n_1\cos\alpha_1 + n_2\cos\alpha_2}, \tag{18}$$

where R_{p} and R_{s} denote the reflection coefficients of p-polarized and s-polarized light, respectively and α_2 is the angle of refraction which is related to α_1 by Snell's law

$$n_1\sin\alpha_1 = n_2\sin\alpha_2. \tag{19}$$

For un-polarized light, the power transmission coefficient of the flat surface is given by

$$T_{\mathrm{air-lens}}(\alpha_1, \alpha_2) = 1 - \frac{1}{2}\left(R_{\mathrm{s}}^2(\alpha_1, \alpha_2) + R_{\mathrm{p}}^2(\alpha_1, \alpha_2)\right). \tag{20}$$

Thus, the power of the light rays that pass through the flat surface of the lens at this infinitesimal area is given by

$$\begin{aligned} dP_2 &= T_{\mathrm{air-lens}}(\alpha_1, \alpha_2) dP_1 \\ &= \frac{P_t(m+1)\cos^m\phi\cos\varphi}{2\pi l^2} T_{\mathrm{air-lens}}(\alpha_1, \alpha_2) r dr d\beta. \end{aligned} \tag{21}$$

These refracted rays then travel to point B, which is at the center of an infinitesimal area on the curved surface of the lens. We assume that the power loss inside the lens is negligibly small. The refracted angle α_4 is related to α_3 by Snell's Law (19). Note that, α_3 and α_4 depend on the coordinates of the point A and the position of the LED. Therefore, the power transmission coefficient of the curved surface is an implicit function of S, the position of the LED, r and β. The derivations of α_3 and α_4 are given in Appendix II. Also note that total internal reflection occurs when α_3 is beyond the critical angle, $\arcsin(n_1/n_2)$ [21]. In this situation, there is no light refracted out of the lens. Although part of these light rays may pass through the lens and

hit the photodetector after multiple internal reflections within the lens, the power of these rays is attenuated severely by reflections, (see (17), (18) and (20)). Therefore, we assume they are lost.

When α_3 is smaller than the critical angle, part of the power of the rays is refracted out of the lens and finally reaches the photodetector array generating the photocurrent for detection. The amount of the power that is refracted out of the lens can be found by exchanging n_1 and n_2 in (17) and (18) and then substituting α_1 and α_2 in (20) by α_3 and α_4, respectively, to give

$$T_{\mathrm{lens-air}}(\alpha_3,\alpha_4) = 1 - \frac{1}{2}\left(R_{\mathrm{s}}^2(\alpha_3,\alpha_4) + R_{\mathrm{p}}^2(\alpha_3,\alpha_4)\right). \quad (22)$$

Therefore, after passing through the lens at B, the power of the rays can be expressed as

$$\begin{aligned} dP_o &= T_{\mathrm{lens-air}}(\alpha_3,\alpha_4)dP_2 \\ &= \frac{P_t(m+1)\cos^m\phi\cos\varphi}{2\pi l^2} \\ &\quad \times T_{\mathrm{air-lens}}(\alpha_1,\alpha_2)T_{\mathrm{lens-air}}(\alpha_3,\alpha_4)rdrd\beta. \end{aligned} \quad (23)$$

As in [7] and [22], the channel gain is defined as the ratio of the power received at the photodetector P_o and the power transmitted by the LED P_t, i.e.

$$T = \frac{P_o}{P_t}. \quad (24)$$

By integrating over all the points for which the rays reach the photodetector, the channel gain can be found. For the case where there is a single photodetector large enough to collect all of the light which passes through the lens

$$\begin{aligned} P_o = &\frac{P_t(m+1)\cos^m\phi\cos\varphi T_{\mathrm{air-lens}}(\alpha_1)}{2\pi l^2} \\ &\times \int\int_{\alpha_3<\arcsin\left(\frac{n_1}{n_2}\right)} T_{\mathrm{lens-air}}(\alpha_3,\alpha_4)rdrd\beta. \end{aligned} \quad (25)$$

Dividing the transmitting power P_t on both sides of (25), we have the channel gain expressed as in (1).

Appendix II

Denote chord DE whose extension intersects with x axis at G as the intersection of the flat surface of the lens and the plane of incidence [21] (see Fig. 2). By the definition of spherical coordinate system, the angle made by DE and the positive x axis is θ (Note that we have assumed that all the light rays coming from the LED are parallel to the light ray reaching the center of the flat surface of the lens.). Therefore, DE can be represented by

$$\frac{y - r\sin\beta}{x - r\cos\beta} = \tan(\theta). \quad (26)$$

Note that the function becomes $y = r\sin\beta$ when $\theta = 0$ or π and $x = r\cos\beta$ when $\theta = \pm\pi/2$. Let the center of chord DE be C. Then the following equation holds by the law of cosines.

$$|AC|^2 + |AB|^2 - 2|AC||AB|\cos(\angle BAC) = |BC|^2. \quad (27)$$

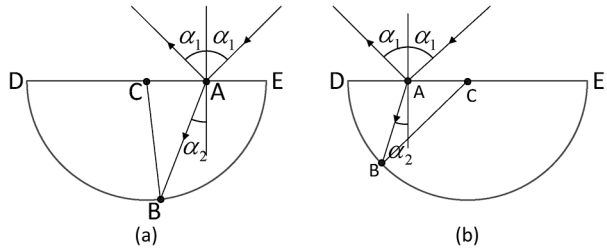

Fig. 11. The plane of incidence of the flat surface of the lens.

By setting $y = 0$ in (26), $|OG|$ equals $r|\cos\beta - (\sin\beta/\tan\theta)|$. Thus, $|OC|$ can be evaluated as

$$\begin{aligned} |OC| &= |OG\sin\theta| \\ &= r\left|\left(\frac{\cos\beta - \sin\beta}{\tan\theta}\right)\sin\theta\right| \\ &= r\,|\sin(\theta-\beta)|, \end{aligned} \quad (28)$$

which leads $|AC|$ can be derived readily as

$$\begin{aligned} |AC| &= \sqrt{|OA|^2 - |OC|^2} \\ &= \sqrt{r^2 - r^2\sin^2(\theta-\beta)} = r\,|\cos(\theta-\beta)|. \end{aligned} \quad (29)$$

$|BC|$ equals $|DC|$ to

$$|BC| = |DC| = \sqrt{|OD|^2 - |OC|^2} = \sqrt{R^2 - r^2\sin^2(\theta-\beta)}. \quad (30)$$

The value of $\cos(\angle BAC)$ depends on the coordinates of A. If A locates to the right of C (as shown in Fig. 11(a)), we have $\cos(\angle BAC) = \sin\alpha_2$. Otherwise, if A locates to the left of C (as shown in Fig. 11(b)), then $\cos(\angle BAC) = \cos((\pi/2) + \alpha_2) = -\sin\alpha_2$. The sign can be determined as follows. Define a vector $\mathbf{r}$ equals $[r\cos\beta, r\sin\beta]^T$. Rotating $\mathbf{r}$ about the z axis by $-\theta$ yields a vector $\mathbf{r}'$ which can be expressed as [23]

$$\mathbf{r}' = \begin{bmatrix} \cos(-\theta) & \sin\theta \\ -\sin\theta & \cos(-\theta) \end{bmatrix}\mathbf{r}. \quad (31)$$

Then, we have

$$\cos(\angle BAC) = \mathrm{sgn}\left(\mathbf{r}'(1)\right)\sin\alpha_2, \quad (32)$$

where $\mathbf{r}'(1)$ denotes the first element of vector $\mathbf{r}'$.

Inserting (29), (30) and (32) into (27), we can solve the function (27) and get its solution as

$$\begin{aligned} |AB| = &\, r\,|\cos(\theta-\beta)|\cos(\angle BAC) \\ &+ \sqrt{r^2\cos^2(\theta-\beta)\sin^2\alpha_2 + R^2 - r^2}. \end{aligned} \quad (33)$$

Next, let's consider the triangle AOB. By the law of cosines, α_3 which equals $\angle ABO$ is given readily by

$$\alpha_3 = \arccos\left(\frac{|AB|^2 + |OB|^2 - |OA|^2}{2|AB||OB|}\right), \quad (34)$$

where $|OB| = R$, $|OA| = r$ and $|AB|$ can be calculated by (33). By Snell's law [21], α_4 is consequently given by $\arcsin((n_2\sin\alpha_3)/n_1)$.

APPENDIX III

Proof of Theorem II: The vector $\mathbf{r}_{SA}$ which equals $\mathbf{r}_{SO}$ approximately can be expressed readily as

$$\mathbf{r}_{SA} = \frac{[0 - l\sin\varphi\cos\theta, 0 - l\sin\varphi\sin\theta, 0 - l\cos\varphi]^T}{l} = [-\sin\varphi\cos\theta, -\sin\varphi\sin\theta, -\cos\varphi]^T. \quad (35)$$

Note that the vector $[0,0,-1]^T$ in (4) is the normal vector of the flat surface of the lens and $\mathbf{r}_{OB}$ is the normal vector of the curved surface of the lens at point B. By the Snell's Law, the angle made between $[0,0,-1]^T$ and $\mathbf{r}_{AB}$ is α_2. Thus, $\mathbf{r}_{AB}$ can be derived by rotating $[0,0,-1]^T$ around $\mathbf{n}_1$ by α_2, where $[0,0,-1]^T$, $\mathbf{r}_{SA}$ and $\mathbf{n}_1$ follow the right-hand rule [23]. This rotation is known as the Euler-Rodrigues (tensor) formula. The resulted vector $\mathbf{r}_{AB}$ can be expressed as

$$\mathbf{r}_{AB} = \mathbf{R}_1 \begin{bmatrix} 0 \\ 0 \\ -1 \end{bmatrix} = \begin{bmatrix} -\sin\alpha_2\cos\theta \\ -\sin\alpha_2\sin\theta \\ -\cos\alpha_2 \end{bmatrix}, \quad (36)$$

where $\mathbf{R}_1$ relates to the axis vector $\mathbf{n}_1$ and the angle α_2 by [23]

$$\begin{aligned}\mathbf{R}_1 &= \cos\alpha_2\mathbf{I} + (1-\cos\alpha_2)\mathbf{A}_1 + \sin\alpha_2\mathbf{B}_1 \\ &= \cos\alpha_2\mathbf{I} + (1-\cos\alpha_2)\begin{bmatrix} \sin^2\theta & -\sin\theta\cos\theta & 0 \\ -\sin\theta\cos\theta & \cos^2\theta & 0 \\ 0 & 0 & 0 \end{bmatrix} \\ &\quad + \sin\alpha_2\begin{bmatrix} 0 & 0 & \cos\theta \\ 0 & 0 & \sin\theta \\ -\cos\theta & -\sin\theta & 0 \end{bmatrix}, \end{aligned} \quad (37)$$

with $\mathbf{I}$ denoting the 3×3 identity matrix and matrix $\mathbf{A}_1$ and $\mathbf{B}_1$ given by [23]

$$\mathbf{A}_1 = \begin{bmatrix} \mathbf{n}_1^2(1) & \mathbf{n}_1(1)\mathbf{n}_1(2) & \mathbf{n}_1(1)\mathbf{n}_1(3) \\ \mathbf{n}_1(2)\mathbf{n}_1(1) & \mathbf{n}_1^2(2) & \mathbf{n}_1(2)\mathbf{n}_1(3) \\ \mathbf{n}_1(3)\mathbf{n}_1(1) & \mathbf{n}_1(3)\mathbf{n}_1(2) & \mathbf{n}_1^2(3) \end{bmatrix} \quad (38)$$

and

$$\mathbf{B}_1 = \begin{bmatrix} 0 & -\mathbf{n}_1(3) & \mathbf{n}_1(2) \\ \mathbf{n}_1(3) & 0 & -\mathbf{n}_1(1) \\ -\mathbf{n}_1(2) & \mathbf{n}_1(1) & 0 \end{bmatrix}, \quad (39)$$

respectively. Therefore, the elements of $\mathbf{r}_{AB}$ are the directional cosines of the straight line AB. Since the straight line AB passes point A, its function in the Cartesian coordinate system can be expressed as

$$\frac{x - r\cos\beta}{-\sin\alpha_2\cos\theta} = \frac{y - r\sin\beta}{-\sin\alpha_2\sin\theta} = \frac{z}{-\cos\alpha_2} = t. \quad (40)$$

As the point B locates on the sphere, its coordinates satisfy that

$$x^2 + y^2 + z^2 = R^2, z < 0 \quad (41)$$

Therefore, inserting (40) into (41), we have the coordinates of point B as shown in (6) and (7). Accordingly, the vector $\mathbf{r}_{OB}$ can be expressed as

$$\mathbf{r}_{OB} = \frac{1}{R}[-t\sin\alpha_2\cos\theta + r\cos\beta, -t\sin\alpha_2\sin\theta + r\sin\beta, -t\cos\alpha_2]^T. \quad (42)$$

Similarly, given $\mathbf{r}_{AB}$, $\mathbf{r}_{BF}$ can be derived by rotating $\mathbf{r}_{OB}$ around $\mathbf{n}_2$ by α_4, where $\mathbf{r}_{OB}$, $\mathbf{r}_{AB}$ and $\mathbf{n}_2$ follow the right-hand rule. Thus, $\mathbf{r}_{BF}$ can be expressed as

$$\mathbf{r}_{BF} = \mathbf{R}_2\mathbf{r}_{OB}, \quad (43)$$

where

$$\mathbf{R}_2 = \cos\alpha_4\mathbf{I} + (1-\cos\alpha_4)\mathbf{A}_2 + \sin\alpha_4\mathbf{B}_2, \quad (44)$$

with matrix $\mathbf{A}_2$ and $\mathbf{B}_2$ given by [23]

$$\mathbf{A}_2 = \begin{bmatrix} \mathbf{n}_2^2(1) & \mathbf{n}_2(1)\mathbf{n}_2(2) & \mathbf{n}_2(1)\mathbf{n}_2(3) \\ \mathbf{n}_2(2)\mathbf{n}_2(1) & \mathbf{n}_2^2(2) & \mathbf{n}_2(2)\mathbf{n}_2(3) \\ \mathbf{n}_2(3)\mathbf{n}_2(1) & \mathbf{n}_2(3)\mathbf{n}_2(2) & \mathbf{n}_2^2(3) \end{bmatrix} \quad (45)$$

and

$$\mathbf{B}_2 = \begin{bmatrix} 0 & -\mathbf{n}_2(3) & \mathbf{n}_2(2) \\ \mathbf{n}_2(3) & 0 & -\mathbf{n}_2(1) \\ -\mathbf{n}_2(2) & \mathbf{n}_2(1) & 0 \end{bmatrix}, \quad (46)$$

respectively. Given the vector $\mathbf{r}_{AB}$ (36) and $\mathbf{r}_{OB}$ (42), the axis vector $\mathbf{n}_2$ can be calculated with (5) as

$$\mathbf{n}_2 = \left[-\frac{r\sin\beta\cos\alpha_2}{R\sin\alpha_3}, \frac{r\cos\beta\cos\alpha_2}{R\sin\alpha_3}, \frac{r\sin\alpha_2\sin(\beta-\theta)}{R\sin\alpha_3}\right]^T. \quad (47)$$

ACKNOWLEDGMENT

The authors would like to thank Mr. J. Yew for the helpful advice on computer simulations.

REFERENCES

[1] T. Komine and M. Nakagawa, "Fundamental analysis for visible-light communication system using LED lights," *IEEE Trans. Consum. Electron.*, vol. 50, pp. 100–107, Feb. 2004.
[2] VLCC, Visible Light Communications Consortium, 2008.
[3] IEEE, IEEE 802.15.7 WPAN Visual Light Communication Study Group, 2008.
[4] D. C. O'Brien, M. Katz, P. Wang, K. Kalliojarvi, S. Arnon, M. Matsumoto, R. J. Green, and S. Jivkova, "Short range optical wireless communications," in *Proc. Wireless World Res. Forum*, 2005 [Online]. Available: http://wg5.wireless-world-research.org/WG5-wp3-Optical_Wireless_Communications-V2005.pdf
[5] J. R. Barry, J. M. Kahn, E. A. Lee, and D. G. Messerschmitt, "High-speed nondirective optical communication for wireless networks," *IEEE Netw. Mag.*, vol. 5, no. 6, pp. 44–54, Nov. 1991.
[6] M. Kavehrad and S. Jivkova, "Indoor broadband optical wireless communications: Optical subsystems designs and their impact on channel characteristics," *IEEE Wireless Commun.*, vol. 10, no. 2, pp. 30–35, Apr. 2003.

[7] L. Zeng, D. C. O'Brien, H. L. Minh, G. E. Faulkner, K. Lee, D. Jung, Y. Oh, and E. T. Won, "High data rate multiple input multiple output (MIMO) optical wireless communications using white led lighting," *IEEE J. Sel. Areas Commun.*, vol. 27, no. 9, pp. 1654–1662, Dec. 2009.
[8] K. D. Dambul, D. C. O'Brien, and G. Faulkner, "Indoor optical wireless MIMO system with an imaging receiver," *IEEE Photon. Technol. Lett.*, vol. 23, no. 2, pp. 97–99, Jan. 2011.
[9] S. Hranilovic and F. R. Kschischang, "A pixelated MIMO wireless optical communication system," *IEEE J. Sel. Topics Quantum Electron.*, vol. 12, no. 4, pp. 859–874, Jul./Aug. 2006.
[10] J. M. Kahn, R. You, P. Djahani, A. G. Weisbin, B. K. Teik, and A. Tang, "Imaging diversity receivers for high-speed infrared wireless communication," *IEEE Commun. Mag.*, vol. 36, no. 12, pp. 88–94, Dec. 1998.
[11] D. C. O'Brien, "Multi-Input Multi-Output (MIMO) indoor optical wireless communications," in *Proc. Signals, Systems Computers, 2009 Conf. Rec. 43rd Asilomar Conf.*, Nov. 2009, pp. 1636–1639.
[12] S. D. Perli, N. Ahmed, and D. Katabi, "PixNet: Interference-free wireless links using LCD-camera pairs," in *Proc. MOBICOM'2010*, 2010, pp. 137–148.
[13] W. Yuan, K. Dana, M. Varga, A. Ashok, M. Gruteser, and N. Mandayam, "Computer vision methods for visual MIMO optical system," in *Proc. CVPRW*, 2011, pp. 37–43.
[14] J. M. Kahn and J. R. Barry, "Wireless infrared communications," *Proc. IEEE*, vol. 85, no. 2, pp. 265–298, Feb 1997.
[15] I. E. Telatar, "Capacity of multi-antenna Gaussian channels," *Eur. Trans. Telecom.*, vol. 10, pp. 585–595, Nov. 1999.
[16] L. Zeng, D. C. O'Brien, H. Le-Minh, L. Kyungwoo, J. Daekwang, and O. Yunje, "Improvement of date rate by using equalization in an indoor visible light communication system," in *Proc. IEEE ICCSC*, 2008, pp. 678–682.
[17] M. J. Langford, A. Fox, and R. S. Smith, *Langford's Basic Photography the Guide for Serious Photographers*, 9th ed. New York, NY, USA: Focal Press.
[18] W. N. Bond, "A wide angle lens for cloud recording," *Philosophical Mag.*, vol. 44, pp. 999–1001, Nov. 1922.
[19] T. Q. Wang, Y. A. Sekercioglu, and J. Armstrong, "Hemispherical lens based imaging receiver for MIMO optical wireless communications," in *Proc. 3rd IEEE Workshop OWC*, Dec. 2012, pp. 1239–1243.
[20] F. R. Gfeller and U. H. Bapst, "Wireless in-house data communication via diffuse infrared radiation," *Proc. IEEE*, vol. 67, pp. 1474–1486, Nov. 1979.
[21] K. D. Möller, *Optics*. Mill Valley, CA, USA: University Science Books.
[22] J. R. Barry, J. M. Kahn, W. J. Krause, E. A. Lee, and D. G. Messerschmitt, "Simulation of multipath impulse response for wireless optical channels," *IEEE J. Sel. Areas Commun.*, vol. 11, no. 3, pp. 367–379, Apr. 1993.
[23] R. M. Brannon, "Rotation, A Review of Useful Theorems Involving Proper Orthogonal Matrices Referenced to Three Dimensional Physical Space," 2002 [Online]. Available: http://www.mech.utah.edu/~brannon/public/rotation.pdf
[24] J. B. Choong and J. Armstrong, "An Optical Wireless Receiver Using A Hemispherical Lens for MIMO Visible Light Communications Systems," Summer Research Project of Monash University, 2013 [Online]. Available: http://titania.ctie.monash.edu.au/mimo-hemis-exp.pdf

Thomas Q. Wang received B.E. degree in electric engineering from Dalian Jiaotong University, Dalian China in 2006 and M.E. and Ph.D. degrees in communication and information systems from Dalian Maritime University, Dalian China in 2008 and 2011, respectively. From 2012, he works as a research fellow with the Department of Electrical and Computer Systems Engineering, Monash University, Melbourne Australia. His research interests include wireless optical communications, cognitive radio, cooperative communications, and multiple-input multiple output (MIMO) technology.

Y. Ahmet Sekercioglu is a member of the academic staff at the Department of Electrical and Computer Systems Engineering of Monash University, Melbourne, Australia. He was the leader of the Applications Program of Australian Telecommunications CRC until the completion of the centre's research activities (December 2007). He has completed his Ph.D. degree at Swinburne University of Technology, B.Sc. and M.Sc. degrees (all in Electrical and Electronics Engineering) at Middle East Technical University, Ankara, Turkey. He lectured at Swinburne University of Technology, Melbourne, Australia for 8 years. Prior to his academic career, he held numerous positions as a research engineer in private industry. He has published 22 journal articles, 2 book chapters, 71 conference papers and has filed 2 patents. His recent research is on distributed algorithms for self-organization in wireless sensor and ad hoc networks, and networked robotics.

Jean Armstrong (M'89–SM'06) received the B.Sc. (First Class Honours) in Electrical Engineering from the University of Edinburgh, Scotland in 1974, the M.Sc. in Digital Techniques from Heriot-Watt University, Edinburgh, Scotland in 1980, and the Ph.D. in Digital Communications from Monash University, Melbourne, Australia in 1993. From 1974–1977 she worked as a Design Engineer at Hewlett-Packard Ltd., Scotland.

In 1977 she was appointed Lecturer in Electrical Engineering at the University of Melbourne, Australia. Since 1977 she has held a range of academic positions at the University of Melbourne, Monash University and La Trobe University. She is currently a Professor at Monash University

Her research interests include digital communications, engineering education, and women in engineering. Most of her recent research has been on Orthogonal Frequency Division Multiplexing (OFDM) and she has published many very highly cited papers and has six fully commercialized patents in this field. Her earlier OFDM work was on RF wireless applications, but in 2005 she recognized the potential for applying OFDM to optical communications. Professor Armstrong has been the recipient of numerous awards including induction into the Victorian Honour Roll of Women, the Peter Doherty for the best commercialization opportunity in Australia in 2006 (joint winner), Institution of Engineers, Australia, Engineering 2000 Award, Zonta International Amelia Earhart Fellowship and Caroline Haslett Memorial Scholarship. She is a Fellow of the Institution of Engineers Australia. She is currently a member of the Australian Research Council (ARC) College of Experts.